AIAA SciTech Forum
23-27 January 2023, National Harbor, MD & Online
AIAA SCITECH 2023 Forum

10.2514/6.2023-0021

A study of Mach wave coalescence using spark sources and large-eddy simulation

William A. Willis III,* John A. Valdez,†
University of Texas at Austin, Austin, Texas 78713, USA

Pierre Pineau‡, Christophe Bogey§
Univ. Lyon, CNRS, École Centrale de Lyon, INSA Lyon, Univ. Claude Bernard Lyon I, Laboratoire de Mécanique des Fluides et d'Acoustique, UMR 5509, 69310 Ecully, France

Charles E. Tinney¶ and Mark F. Hamilton‖
University of Texas at Austin, Austin, Texas 78713, USA

The coalescence of intersecting Mach waves has been proposed as a significant contributor to acoustic waveform steepening in the near field of a jet, thus providing a potential cause for the observation of more steepened waves in a laboratory-scale jet than predicted by effective Gol'dberg numbers [Baars et al., J. Fluid Mechanics 749 (2014); Fiévet et al., AIAA Journal 54, 254 (2016)]. Recent numerical simulations have demonstrated that the coalescence process can lead to increased steepening [Willis et al., AIAA SciTech Forum (2022)]. Schlieren imaging of a laboratory-scale, Mach 3 jet flow has been used for comparison with simulations based on reduced-order models, but additional examples of coalescing waves were desired that did not depend on turbulence for wave generation. Thus, two experiments have been designed using spark generated waveforms that intersect, either after reflection from a rigid surface or after emanating from a 3D-printed enclosure. Schlieren images and microphone measurements allow for analysis of these waveforms to examine steepening behavior. Additionally, large-eddy simulation (LES) of the same Mach 3 jet flow presents an opportunity to compare behavior of intersecting Mach waves with prior simulations and experimental results. A machine learning algorithm has been trained using transfer learning and then applied to the LES pressure data to identify waveforms of interest for further analysis of coalescence.

I. Introduction

As a component of turbulence mixing noise, Mach waves form when the convective speed of the large-scale turbulent structures is greater than the sound speed of the neighboring gas. Mach waves produce significant levels of noise for high Mach number supersonic jets, thus making them a source of interest for various jet noise phenomena [1]. Cumulative nonlinear waveform distortion causes Mach waves of sufficient amplitude to undergo steepening, even to the point of forming shocks. Efforts to understand these local distortion effects in the context of jet noise are found in the numerical studies by Nichols et al. [2], Buchta and Freund [3] and Pineau and Bogey [4, 5]. These distorted waveforms produce the sound referred to as 'crackle' that has been a topic of scientific interest for several decades, beginning with the seminal work of Ffowcs Williams et al. [6].

According to the theoretical framework first developed by Baars et al. [7] and Baars et al. [8], there is a discrepancy between the mechanisms that cause distorted acoustic waveforms to form from large full-scale jet engines [9] versus the ones produced by their smaller, laboratory-scale, counterparts [8]. In laboratory-scale jet noise measurements of Fiévet et al. [10], Mach wave steepening was shown to exceed the levels predicted based on theoretical estimates for shock formation distance and effective Gol'dberg number [8, 11]. A potential cause for this phenomenon was

*Graduate Research Assistant, Applied Research Laboratories and Walker Department of Mechanical Engineering, william.willis@utexas.edu (Corresponding Author).
†Engineering Associate, Applied Research Laboratories; john.valdez@arlut.utexas.edu. Member AIAA.
‡Postdoctoral Fellow, now Research Engineer at EDF RD, pierre.duval-pineau@edf.fr
§CNRS Research Scientist, christophe.bogey@ec-lyon.fr. AIAA Senior Member and Associate Fellow.
¶Research Scientist, Applied Research Laboratories; cetinney@utexas.edu. Associate Fellow AIAA.
‖Professor, Applied Research Laboratories and Walker Department of Mechanical Engineering; hamilton@mail.utexas.edu.

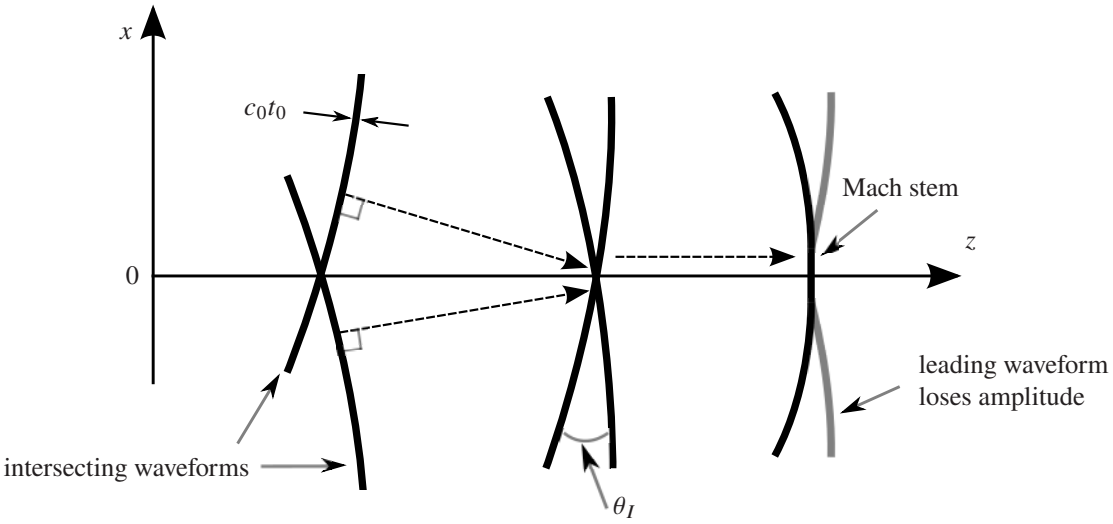

Fig. 1 Illustration of coalescence process.

attributed to coalescence between waveforms, as illustrated in Fig. 1. When waves intersect in the free field while propagating at small angles relative to one another, they have the potential to merge into a waveform of larger amplitude. A recent investigation by Willis et al. [12] showed that the increase in amplitude due to coalescence was capable of enhancing waveform steepening when compared to individually propagating waveforms that do not coalesce. The resultant increase in the degree of steepening was shown to depend on intersection angle θ_I between waveforms, waveform duration t_0, and geometric spreading. A reduced-order model of the simulated waveforms was compared to schlieren images of intersecting waveforms in the sound field of Mach 3 jet flow, with both demonstrating similar modal behavior.

The present study continues the prior work of Willis et al. [12] in investigating Mach wave coalescence. Although Mach wave coalescence was successfully captured in the schlieren images of a laboratory-scale supersonic jet flow, the source of those Mach waves was from the unsteady turbulence, which can vary significantly due to its stochastic nature. It was determined that a spark source could provide a controlled waveform generation mechanism as an alternative. In addition, the relationship between schlieren intensity and pressure is not trivial, and so a study that deduces the behavior of coalescing waves in a jet's near field from a measurement of pressure is more favorable. Experimental verification of increased steepening due to coalescence, along with dependence on parameters determined by the prior work's Khokhlov-Zabolotskaya-Kuznetzov (KZK) equation simulations, was also desired.

An outline of this study is as follows. We begin with simple experiments comprising a spark source and standard laboratory instruments (high speed digital schlieren and acoustic microphones) to study waveform coalescence and its effect on steepness under controlled conditions. Schlieren images are used to construct reduced-order models of waveform coalescence using proper orthogonal decomposition (POD) in translating coordinates. Next, the pressure data of a large-eddy simulation (LES) of a high Mach number supersonic jet are evaluated using a coalescence detection algorithm, similar to what was performed by Willis et al. [12] using schlieren images. The analysis of the spatially and temporally resolved LES sound field is then extended using modern machine learning algorithms to explore the utility of these techniques in capturing waveform coalescence. The findings are part of a larger effort to understand the effect of waveform coalescence in the sound field of high Mach number supersonic jets, and the use of machine learning techniques for capturing and tracking these events.

II. Laboratory Measurements of Waveform Coalescence

The test campaign discussed here comprised measurements of different waveforms that were generated using a spark source. Spark sources are an effective way of studying sound waves in air and have been used elsewhere to produce repeatable, spherically-spreading N waves with sufficient amplitude to undergo cumulative nonlinear distortions [13]. The spark generator is a model GTS 51-4 made by Grozier Technical Systems Inc. and generates a triggered spark by discharging a high voltage capacitor from two electrodes separated by an air gap. The acoustic waveform produced by

this spark source is spherical and has been verified using schlieren imaging by Hay et al. [14] and Tinney et al. [15]. It is believed that the contribution of coalescence is more important for cylindrically or spherically spreading waves than for non-spreading ones, as it allows these waves to overcome the decrease in amplitude due to spreading [12], thereby favoring nonlinear propagation effects. Two experiments were designed in order to study intersecting and coalescing waveforms. The first uses the spark source in open air and with an acoustically reflective surface to induce coalescence between incident and reflecting waves, while the second encloses the spark source in a cavity with two equal diameter vents. The vents effectively split the initial spark-generated waveform into two so that various waveform interaction phenomena can be studied. Both schlieren imaging and single point microphone measurements are employed to capture waveform interactions and are scrutinized using indicators that quantify waveform steepness. Schlieren images are in turn decomposed in order to evaluate the low-dimensional makeup of the waveform coalescence process, which allows for a direct comparison to reconstructed KZK and schlieren images shown in the previous study [12]. Detailed descriptions of the experimental arrangement and apparatus are as follows.

A. Reflecting Surface Experiment

The first of these spark source studies relies on the fact that symmetrically-intersecting waves in free air share the same boundary condition on their axis of symmetry as do waveforms propagating at grazing incidence to a rigid surface. Karzova et al. [16] used this kind of setup to model Mach stem formation along a rigid surface in order to study intersecting shock waves, while the present work focuses on the steepness of the intersecting waveforms. Here, time-resolved images of waveform behavior were captured using a double-pass Schlieren system comprising a LUMINUS CBT-120 Green 510-540 nm LED light source, a gold-coated 31.75 cm diameter parabolic mirror, and an i-SPEED 726 monochromatic digital camera. A vertical razor blade cutoff was used to obtain horizontal pressure gradients parallel to the coalescence axis. The double-pass setup doubles the amount of refraction experienced by the light, thereby increasing sensitivity. The mirror has a 254 cm focal length to reduce astigmatism effects and was mounted directly behind the spark source with sufficient distance from the reflecting surface and spark source to avoid errant acoustic reflections. Images were recorded uninterrupted at 100 000 fps using 1064×268 pixel resolution and a magnification of 0.3267 mm/pixel. A diagram depicting the schlieren system is provided in Figure 2a.

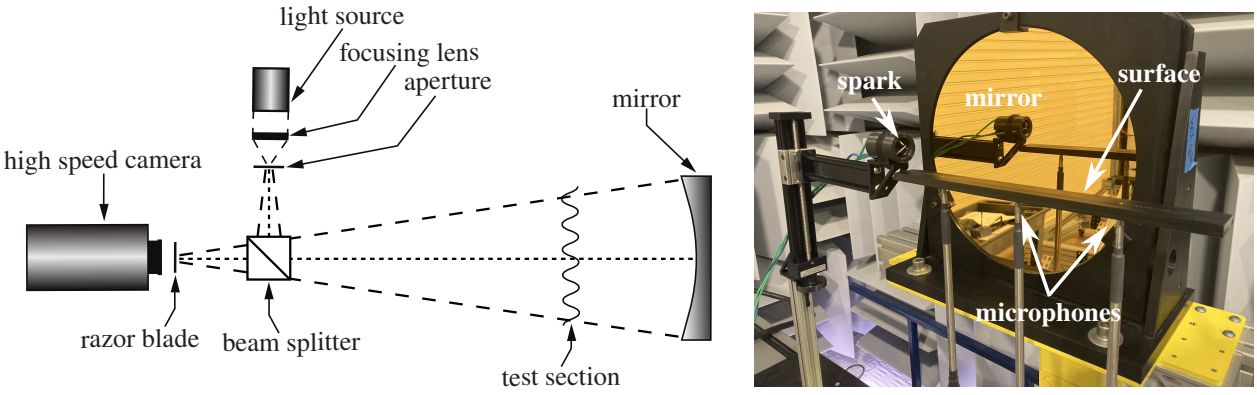

a) b)

Fig. 2 a) Diagram of double-pass schlieren system and b) image of the schlieren system with reflecting surface and microphone array in the Gas Dynamics Laboratory at ARL:UT.

Pressure waveform amplitudes were captured using an array of three microphones embedded in the reflective surface and with the protective grid caps pushed flush to reduce reflections. The microphones used were G.R.A.S. model 46DD eighth-inch pressure-field microphones, having a 174 dB dynamic range and a frequency bandwidth of 140 kHz with ±3 dB uncertainty. Analogue signals were digitized at 500 kHz without low-pass filtering; the microphones themselves function as the low-pass filter. The positions of these three microphones, relative to the center of the spark source are provided in Table 1. The spark source was mounted to the reflecting surface with free-standing wires in order to reduce reflections from surfaces other than the rigid plane. The rigid plane itself was fabricated from plastic and machined to a smooth, acoustically reflective finish. A schlieren image in Fig. 3 depicts the setup and illustrates the propagation of an incident and reflected waveform along the rigid surface. Note that the sample image is shown

microphone number	1	2	3
distance from source [cm]	6.7	16.6	26.8
$\bar{\gamma}(\dot{p})$ with surface (first compression)	1.46 ± 0.045	1.61 ± 0.009	1.51 ± 0.017
$\bar{\gamma}(\dot{p})$ without surface (first compression)	1.12 ± 0.029	1.54 ± 0.013	1.24 ± 0.001
$\bar{\gamma}(\dot{p})$ with surface (second compression)	−0.519 ± 0.057	−0.580 ± 0.034	−0.803 ± 0.043
$\bar{\gamma}(\dot{p})$ without surface (second compression)	−1.43 ± 0.040	−0.896 ± 0.044	−1.15 ± 0.037

Table 1 Microphone locations along with calculated values for skewness of the pressure time derivative from an average of 10 trials with and without the reflective surface. Provided uncertainties represent standard error.

without subtracting a waveform-free background image so that the reflecting surface remains visually distinguishable from other parts of the background. The reflected waveform is clearly present, along with an increase in intensity where the reflected and incident waveforms overlap. This suggests that the pressure gradient at the intersection point is larger relative to other positions along the waveform. To verify that this is true, additional microphone measurements were performed without the reflecting surface in order to provide a direct comparison to non-intersecting waveforms.

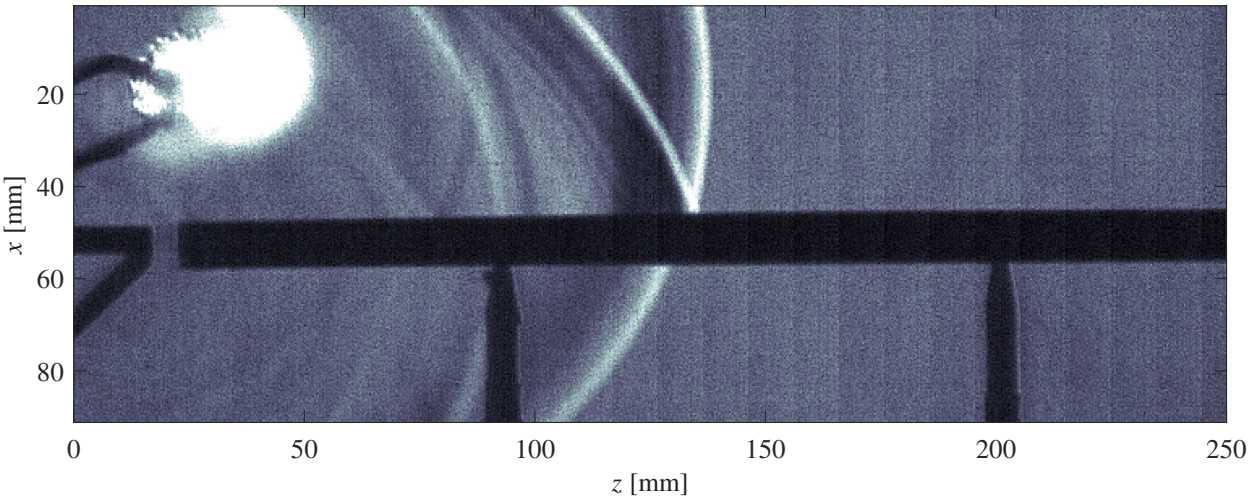

Fig. 3 Schlieren image at 100 000 fps of a spark-generated wave with both incident and reflected waves.

In Fig. 4, a sample of the measured pressure waveforms are presented with and without the effect of the reflecting surface. The average peak amplitude of the waveforms from the reflecting surface was 2.0 kPa less than double the average amplitude of waveforms without the surface, a difference attributed to either the peak occurring between microphone samples, or increased absorption with shock formation in the higher-amplitude waveform. The increase in pressure compared to the surface-free case indicates that the waves did not shock prior to coalescing, since the coalescence of shocked waveforms would result in one shock merging with the other without gaining amplitude [17]. To characterize steepening, the commonly used metric known as skewness of the pressure time derivative was applied, and is defined as follows:

$$\gamma(\dot{p}) = \frac{\overline{\left(\dot{p} - \overline{\dot{p}}\right)^3}}{\dot{\sigma}^3}, \tag{1}$$

with $\dot{\sigma}$ being the standard deviation of $\dot{p} = \partial p/\partial t$. Derivative skewness is zero for a perfectly symmetric waveform and increases when asymmetry is introduced through waveform steepening, thus making it a useful indicator of crackle [9].

Skewness values are provided in Table 1 and are based on an average of ten spark trials with and without the surface. Derivative skewness was calculated over a time window from −10 to 30 μs, with the peak of the first arrival aligned at 0 μs, to compare the slopes of the initial compression and expansion of the N wave. For all three microphones, the waveforms measured using the acoustically reflective surface have higher derivative skewness, and are thus experiencing

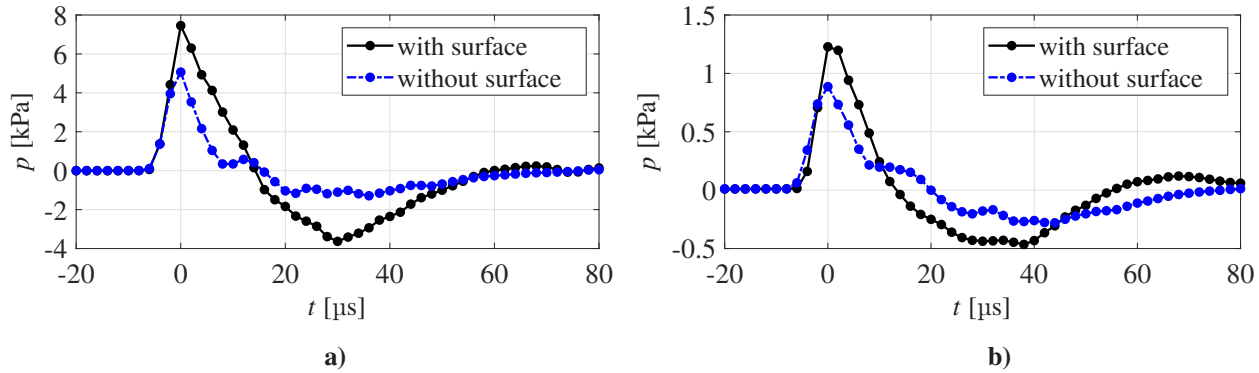

Fig. 4 Pressure-time series recorded by microphones a) at 6.7 cm and b) at 26.8 cm from the spark with and without the reflective surface.

a higher degree of steepening. This trend was consistent across all ten trials, along with Microphone 2 demonstrating the highest skewness. Some caution is warranted in that the microphone diaphragm size and response times can affect measured rise times (see Yuldashev et al. [18]). To account for this, derivative skewness calculations were re-evaluated over a time window from 0 to 50 μs, allowing for comparison of the N wave's expansion to its second compression while still neglecting later portions of the waveform that exhibit relaxation-induced asymmetry. The findings are reported in Table 1, where those propagating with the surface still exhibit consistently higher skewness levels than those propagating in the free field. The resulting skewness values are negative since the expansion process exhibits a greater slope than the second compression, but that second compression is still steeper for waveforms with the surface than without. This provides compelling evidence that coalescence between neighboring waveforms, modeled using the reflecting surface, will increase waveform steepening and cumulative nonlinear distortion effects. Based on these findings, a second series of tests were conducted by utilizing the high-speed schlieren system without the presence of the microphones in order to address concerns regarding the bandwidth limitations imposed by the microphones. Diffraction effects from microphone surfaces can also be avoided using schlieren imaging.

B. Split Waveform Experiment

In order to generate two spherically propagating waveforms without the use of an acoustically reflective surface, a simple wave splitter was designed and fabricated using 3D printing methods. The general design is shown in Fig. 5a while its location, relative to the schlieren mirror, is shown in Fig. 5b. Accurate positioning of the wave splitter, relative to the microphone array, was controlled by fastening the wave splitter to a linear traverse. The spark generator was then placed inside the wave splitter (as seen in Fig, 5a) so that spark-generated waveforms were incident on two tubes inclined at 30 deg to the axis of symmetry and with equal diameters of D_h = 10 mm. Both tubes vent to the atmosphere thereby generating two acoustic sources at identical times with a 30 mm separation distance. The wave splitter is fabricated from Polyactic Acid with a 40% infill, so it is assumed to have rigid boundaries compared to air. When the two waveforms emerge from the tubes, they propagate spherically and unrestricted as they begin to intersect and coalesce.

To examine waveform behavior, the same double-pass schlieren system described in Section II.A was employed here. Figure 6a shows a schlieren image of intersecting waveforms after emerging from the wave splitter. For the coordinate axes, z refers to the direction of propagation and x to the perpendicular axis as defined in Fig. 1. The sample image is shown without subtracting a waveform-free background image so that the relative size of the wave splitter can be observed. Internal acoustic reflections produced by the spark source are seen propagating after the arrival of the main acoustic waveform, but with sufficient delay to allow waveform coalescence to be examined without the effects of spurious noise.

In order to study the behavior of single, non-coalescing waveforms (to be compared to coalescing waveforms), the bottom vent of the wave splitter was plugged with a soft cloth. A schlieren image of this is shown in Fig. 6b. The illustration demonstrates how the single waveform is similar in amplitude to the individual intersecting waveforms shown in Fig. 6a, with differences attributed to variations in the spark source amplitude between trials.

Acoustic pressure waveform amplitude is then measured by placing the same three microphones in the field as

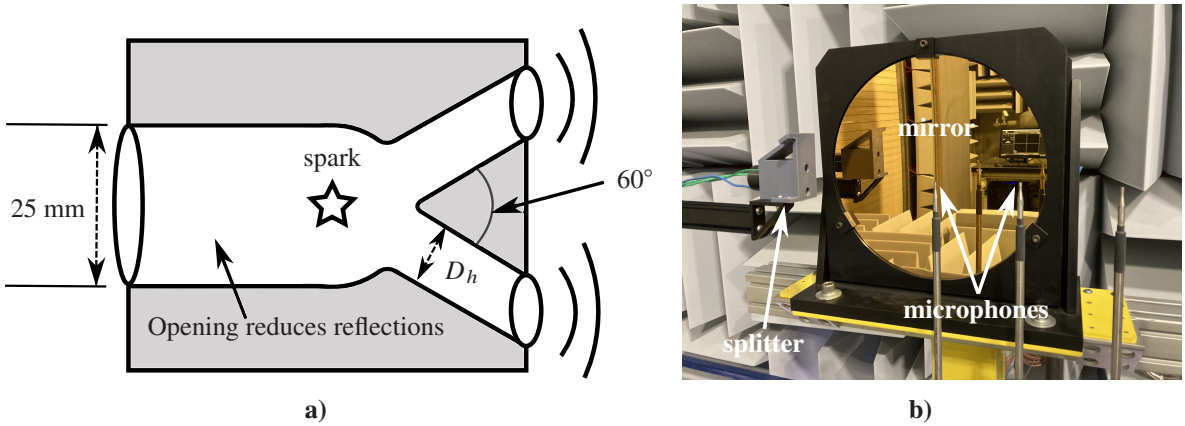

Fig. 5 a) Overview of spark wave splitter. b) Image of the schlieren system alongside the wave splitter and microphone array in the Gas Dynamics Laboratory at ARL:UT.

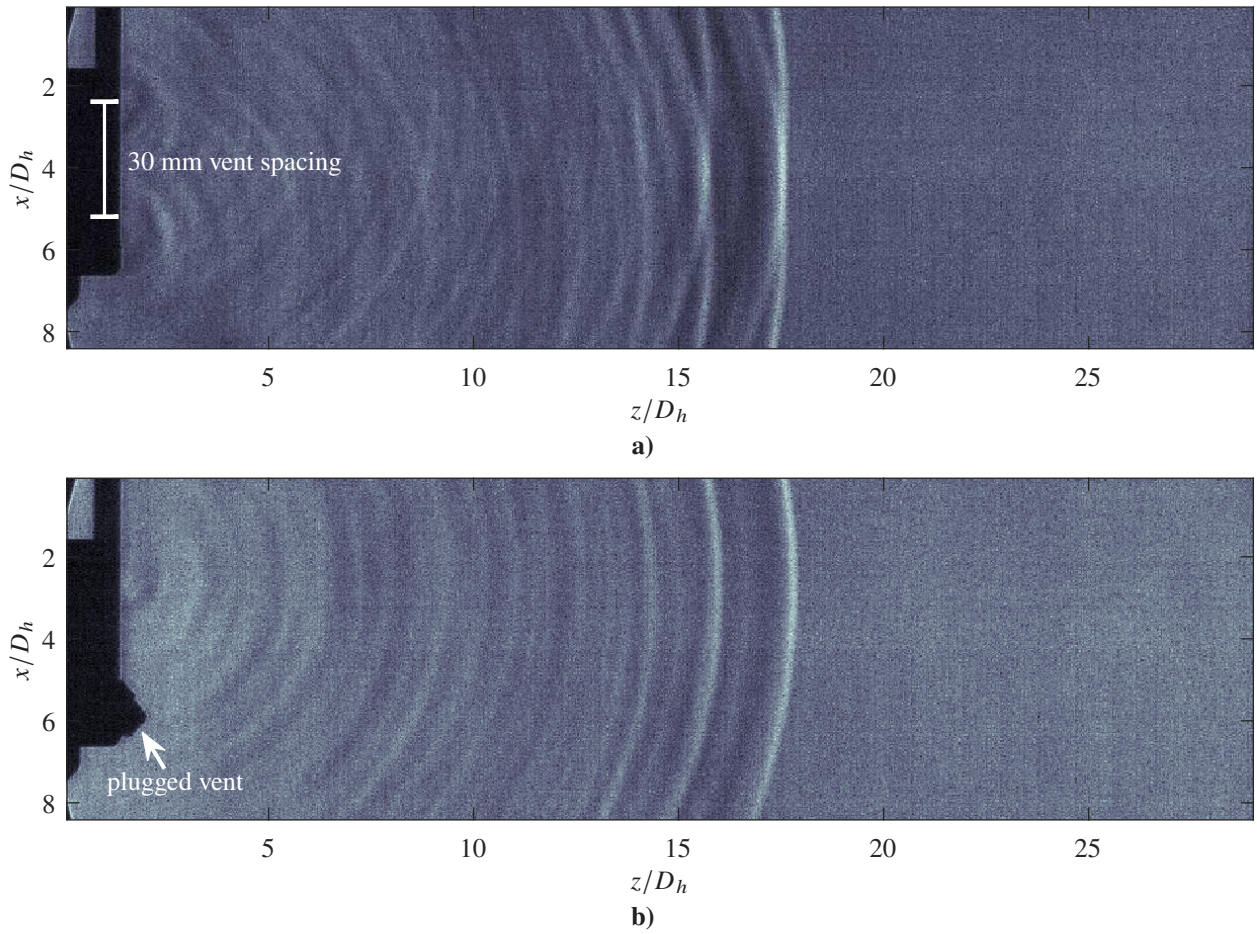

Fig. 6 Schlieren images at 100 000 fps of a) coalescing waves emitted from both openings in the wave splitter and b) a single wave from the upper opening in the wave splitter.

shown in Fig. 5b. Microphone diaphragms were aligned with the axis of symmetry using the schlieren system as a guide. This is an important step because the largest increases in amplitude due to coalescence occurs along this axis, and is where the largest changes in steepening are expected to occur. Microphone measurements for coalescing

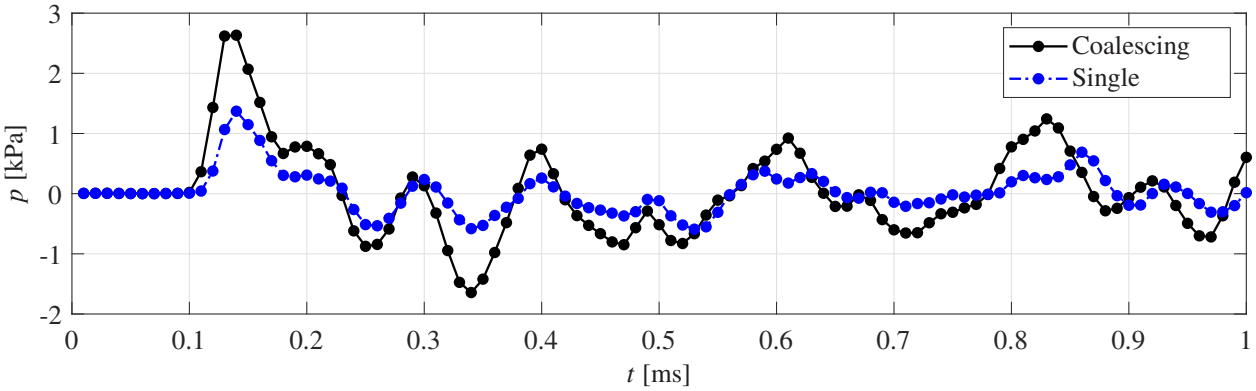

Fig. 7 Pressure-time series recorded by a free standing microphone at 5.5 cm along the axis of symmetry for single and coalescing waveforms emitted by the wave splitter.

waveforms, and a single waveform along the same axis, are shown in Fig. 7a for the nearest microphone located 5.5 cm from the wave splitter. One can see that the coalescing waveforms are very approximately twice the amplitude of the single waveform (recorded peak pressures of 1.37 kPa and 2.63 kPa, respectively), as expected. This difference can be attributed to the earlier concerns regarding microphone sampling and absorption. However, the coalescing waveforms for some measurements exhibited ampltidues greater than double the single waveform amplitude, which would suggest that variations in the spark source are a factor. Note that the N waves recorded at the start of each arrival are not as clean as those recorded by Lipkins and Blackstock [13]. Given their consistency between the coalescing and single waveform trials, it is evident that these ripples are produced by acoustic reflections from inside the wave splitter, including potential low-level reflections from roughness of the printed surface, and that the rise and fall of the initial wavefront is not corrupted by these reflections.

C. Analysis in Translating Coordinates

As with prior analysis of Mach waves [12], the trajectory of intersecting waveforms are tracked using translating coordinates. A demonstration of this is shown in Fig. 8, where spatially resolved windows form boundaries that translate with the coalescing waveforms to form a collection of partial fields of schlieren intensity $\xi(t, \mathbf{x}(t))$ that are both space and time dependent. Waveform propagation speeds were estimated to be 10.5 pixels/frame based on the sound speed for air of $c_0 = 343$ m/s and an image magnification of 0.3267 mm/pixel. Doing so aligns the propagating waveforms with the centers of the translating frames. A sample set of partial fields corresponding to coalescing waveforms is shown in Fig. 9.

In order to compare steepening between the two cases, it is important to recognize that schlieren intensity is more closely a function of the pressure gradient in the direction of the cutoff, as shown by Hay et al. [14]. As a pressure waveform steepens, the pressure gradient is expected to exhibit a higher amplitude, shorter duration peak that shifts forward in time. Although spherical spreading counteracts any increase in schlieren intensity due to steepening, the waveforms in Fig. 9a for the intersecting waveform case display higher amplitude, sharper peaks than those in Fig. 9b for the single waveforms, which is a sign of increased steepening.

A quantitative metric for characterizing changes in waveform steepness is developed by comparing the ratio of peak positive schlieren intensity to peak negative schlieren intensity, $I_{+,\max}/I_{-,\max}$. This approximates the ratio of slopes of the front of the pressure waveform to the slope of its tail, given that it is schlieren intensity and not pressure. Higher ratios correspond to steeper waveforms. For intensities measured at $z/D_h = 5.65$, the waveforms are found to have ratios of $I_{+,\max}/I_{-,\max} = 2.40 \pm 0.18$ (standard error) for the intersecting waveforms, and 1.77 ± 0.14 for the single waveforms, averaged over 5 trials for each case. This supports the conclusion that the captured intersecting waveforms are steepening while coalescing. At further distances, the noise floor of the digital camera is comparable to the peak negative intensity for the single waveforms, making this metric less reliable. It is also uncertain where these waveforms transition from being dominated by distortion effects to being dominated by relaxation and geometric spreading, which would affect the peak intensity ratios, and so additional analysis with the schlieren images is warranted.

To further the analysis, a proper orthogonal decomposition of these partial fields is used in order to compare the spatial makeup of the low-order modes of these coalescing waveforms to our findings reported in previous studies.

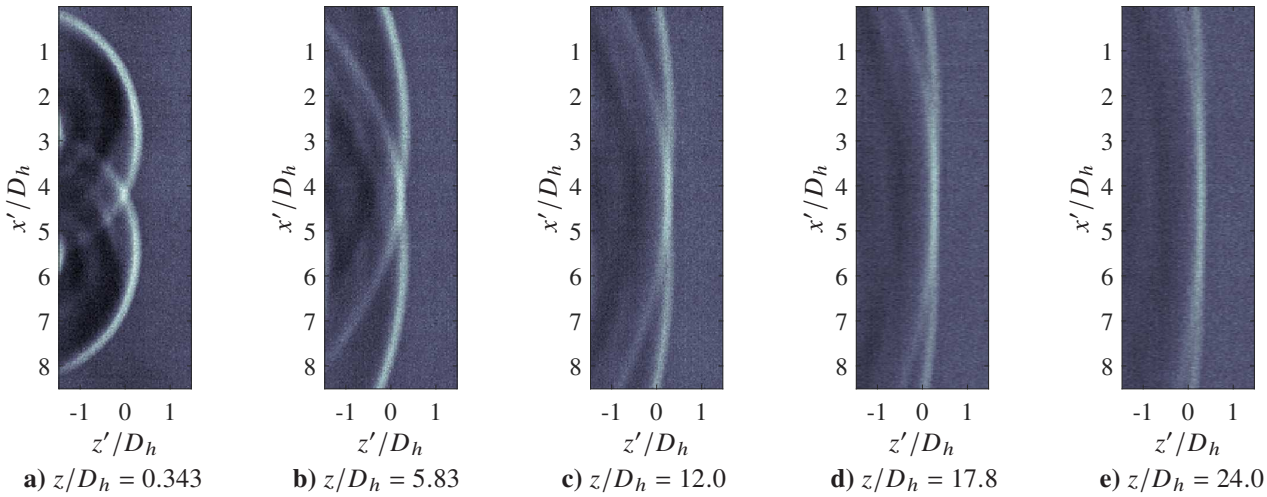

Fig. 8 Schlieren images of coalescing waves from the wave splitter using translating frames.

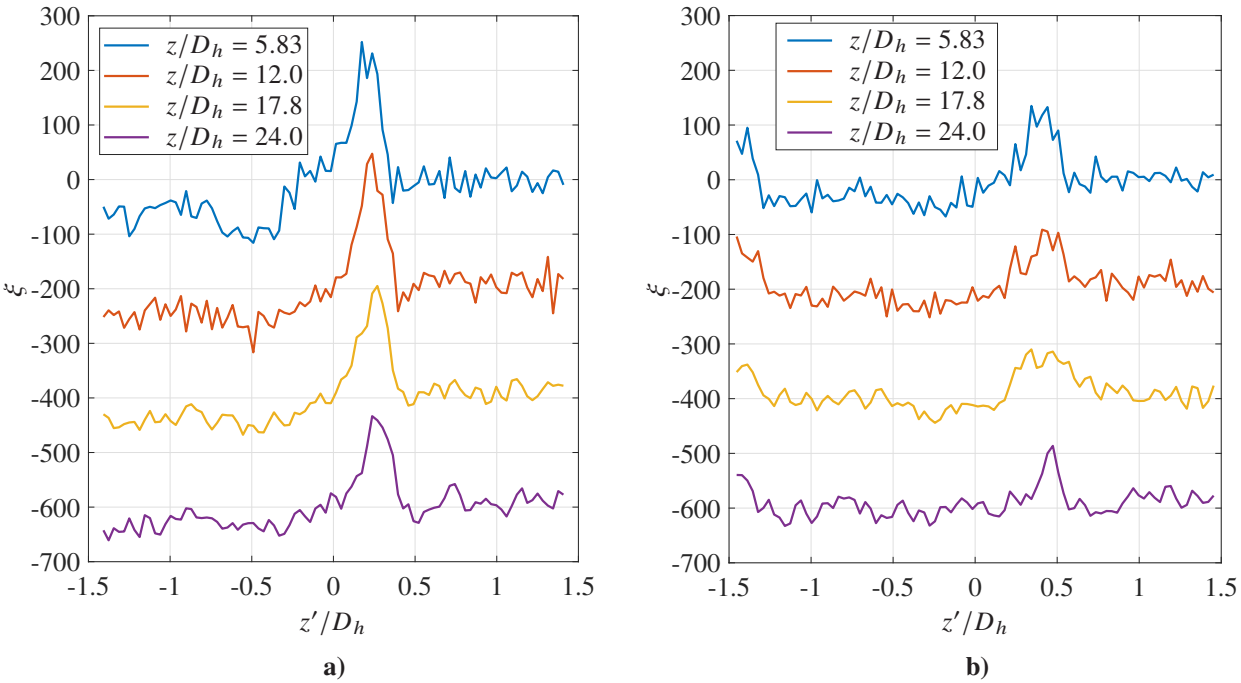

Fig. 9 Schlieren intensity of spatially evolving waveforms captured in the translating frames for the a) coalescing and b) single waveform cases.

A detailed outline of the POD technique is easily found in the open literature (see Lumley [19], Berkooz et al. [20], Tinney et al. [21] and Tinney [22]), whereas its development in the context of translating coordinates is described by Willis et al. [12]. For the present analysis, the moving windows comprise dimensions of $(z' \times x') = (60 \times 228)$ pixels, traversed to $M = 68$ points along the propagation path resulting in 68 partial fields with 13680 spatial points. The

spatial rank $\mathbf{x}(t) = z' \times x'$ exceeds that in time M, such that the preferred form for the kernel preserves time as follows:

$$\begin{aligned}\langle \xi_{t\mathbf{x}}, \xi_{t'\mathbf{x}} \rangle_{tt'} &= \sum_{\mathbf{x}} \xi(t, \mathbf{x}(t)) \xi^*(t', \mathbf{x}(t')) \\ &= R(t, t') \\ &= R_{tt'} \end{aligned} \tag{2}$$

where brackets define the inner product operation and the subscript segregates the space comprising the inner product operation from the space that is being preserved. The following eigenvalue problem is then solved,

$$\langle R_{tt'}, \Phi^n_{t'} \rangle_t = \Lambda^n \Phi^n_t \tag{3}$$

and produces a linearly dependent set of scalar eigenvalues Λ for $R_{tt'}$ with corresponding eigenvectors Φ. POD expansion coefficients represent the dynamics of the individual modes and are obtained using the same inner product operation $a^n_{\mathbf{x}} = \langle \xi_{t\mathbf{x}}, \Phi^n_t \rangle_{\mathbf{x}}$, and whose mean square values are the eigenvalues themselves. In our analysis, eigenvalues will be presented as both fractions of total resolved energy,

$$F^n_\lambda = \frac{\Lambda^n}{\sum_{n=1}^{M} \Lambda^n} \tag{4}$$

and by their cumulative sum,

$$C^m_\lambda = \frac{\sum_{n=1}^{m} \Lambda^n}{\sum_{n=1}^{M} \Lambda^n} \tag{5}$$

so that $C^m_\lambda = 1$ when $m = M$.

From the reconstructed kernel, the spatial modes of the intersecting waveforms generated by the spark source are examined and compared to those obtained for KZK simulations and Mach waves of Willis et al. [12]. Using a collection of partial fields from one spark trial as an example, images of the spatial topology of the first four most energetic POD modes are presented in Fig. 10. The first mode closely resembles the behavior of the first mode of both the Mach wave schlieren images and the KZK simulations reported by Willis et al. [12], while the second through fourth modes show similar topologies to those in the previous study but with reversed phase. The topologies of the second through fourth modes are quite similar to those from the KZK simulations, with increased curvature away from the axis of symmetry due to the fact that the spark source generates spherically spreading waves, compared to the plane waves simulated in the KZK analysis.

Comparisons of the first four POD modes along the axis of symmetry, where coalescence and waveform steepening is greatest, are presented in Fig. 11a. These spatial modes are plotted separately, and as a cumulative sum of their waveforms. Prior analysis of coalescing waveforms using both KZK simulations and schlieren images of Mach waves showed how the second mode was associated principally with waveform steepening [12]. Here, the second mode of the spark-generated waveforms also contributes to increased steepening of the cumulative waveform. However, these spark-generated waveforms have smaller amplitudes than those simulated by the KZK equation, and thus experience less steepening, which affects the shape of the second mode axial waveforms in Fig. 11a. The second mode is also examined in Fig. 11b, depicting evolution of the on-axis waveform with the translating frame that follows the propagating waves. The second mode experiences a significant decrease in amplitude for the frame centered at $z/D_h = 5.83$, which can be seen in Fig. 8 to correspond to the early stages of coalescence and a potential disruption in steepening.

Through these simple experiments comparing a spark source, wave splitter and acoustically reflective surface, it was possible to verify that coalescence has a noticeable impact on waveform steepening. The next step is to extend this same analysis to the sound field of a real jet flow, which was performed by Willis et al. [12] using time-resolved schlieren images of a Mach 3 jet. The shortcoming of using schlieren methods is that it is not an actual measure of pressure, but rather a line-of-sight integration of its second spatial derivative. Therefore, a large-eddy simulation of the same Mach 3 jet flow will be leveraged, which comprises a spatially and temporally resolved database of the full velocity, pressure and density fields. Doing so should complement the findings reported here using the simple spark source, as well as the findings of Willis et al. [12].

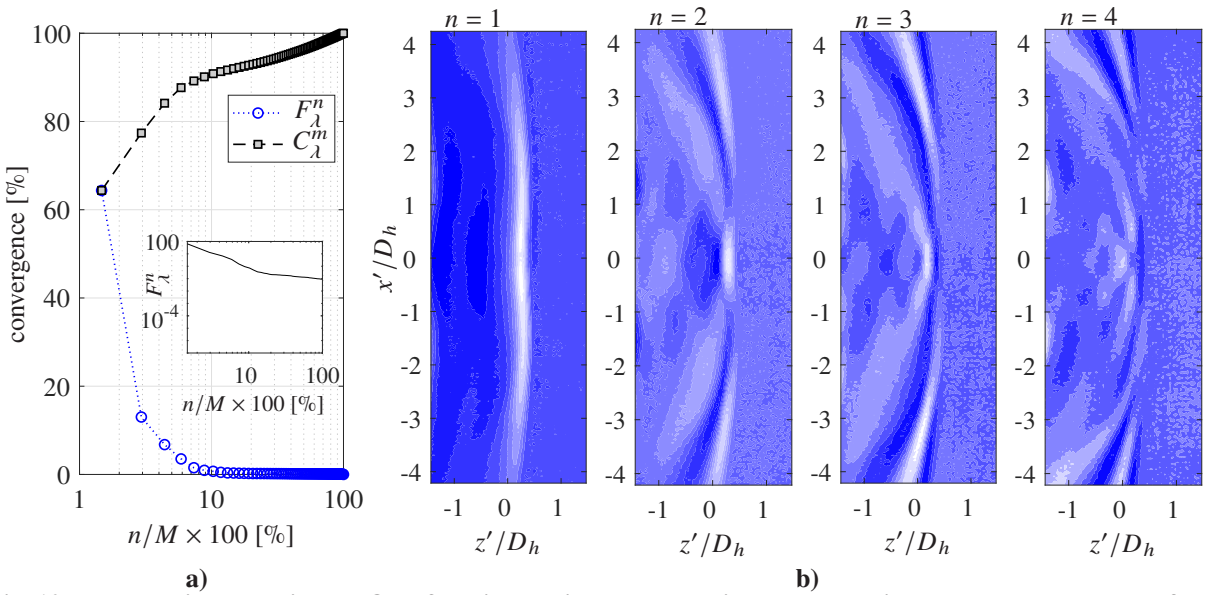

Fig. 10 Translating coordinate POD of schlieren windows capturing the coalescing spark-generated waveforms. a) Eigenvalue convergence. b) Spatial makeup of the first four POD modes.

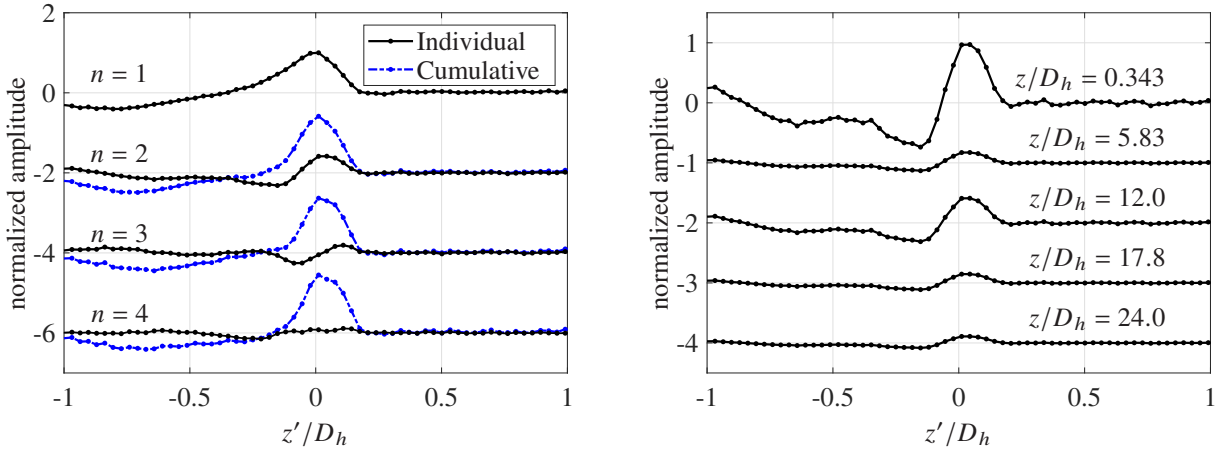

Fig. 11 a) First four translating coordinate POD mode shapes along $x' = 0$, along with cumulative sum of modes. b) Evolution of second POD mode along the $x' = 0$ axis at selected propagation distances.

III. Large Eddy Simulation (LES)

The simulated jet examined for this analysis is the jet computed using large-eddy simulation by Pineau and Bogey [5], which in turn was based on the physical jet used in the studies by Baars et al. [23], Fiévet et al. [10] and Willis et al. [12]. The previous study by Pineau and Bogey [5] used the LES to examine shock coalescence rather than the coalescence of steepened waveforms without shocks, which are the focus of the present study. This is an important distinction in that during shock coalescence, the larger amplitude shock will merge with the smaller one without gaining amplitude [17], while in contrast waveforms without shocks will combine into a higher amplitude waveform when coalescing [12].

The jet is perfectly expanded and exits from a straight-pipe nozzle with a centerline velocity of $U_j = 615$ m/s corresponding to a gas dynamic Mach number of $M_j = 3$. The jet diameter for the simulation was defined as $D_j = 2r_0 = 0.7$ mm, resulting in a diameter-based Reynolds number of 2×10^5. The LES was performed by solving

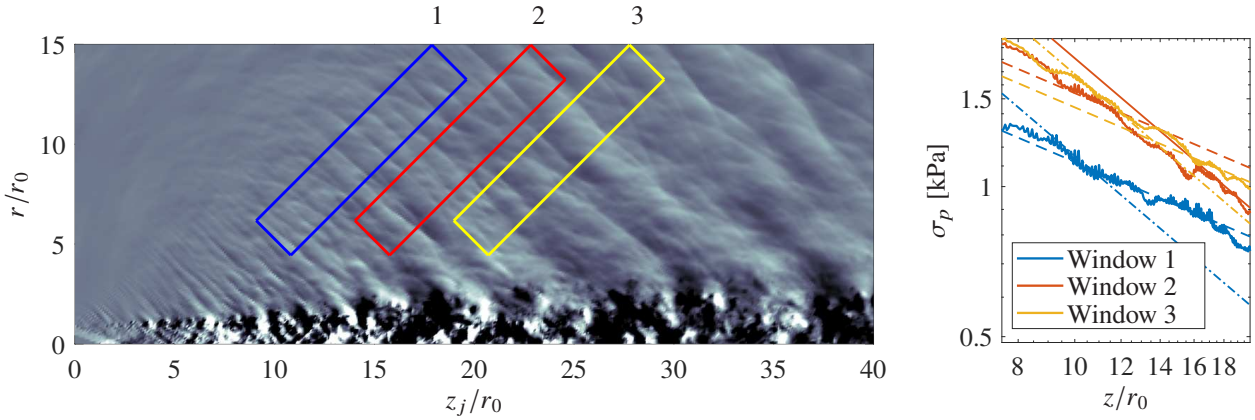

Fig. 12 LES model of a Mach 3 jet flow from Pineau and Bogey [5]. a) $\phi = 0$ deg plane at $tu_j/D_j = 39.0$ with highlighted windows for subsequent analysis. b) RMS pressure (solid lines) calculated along window centerlines and compared to cylindrical (dashed) and spherical (dashed-dot) decay rates.

the filtered compressible Navier–Stokes equations in cylindrical coordinates using high-order finite difference schemes. The computational domain extends to $z_j = 35D_j$ in the axial direction and $r = 7.5D_j$ in the radial direction, for a total of 325 million points [5]. Here, z_j denotes the direction of the jet axis to differentiate from the wave propagation direction z as established in Section II. The resulting spatial resolution was $dz_j = dr = 0.05r_0$, with a time resolution of $dt = 0.11$ μs and corresponding cutoff Strouhal number of $\mathrm{St} = fD_j/U_j = 10$. Although the LES results had been previously used by Pineau and Bogey [5] to propagate acoustic waveforms into the far field, for this analysis we examine the near field of the jet, as that is the region of primary interest, where the onset of steepening due to coalescence is believed to contribute to the crackle phenomenon.

A slice through the r-z_j plane of the LES jet flow at an azimuthal angle of $\phi = 0$ deg is used to compare to the coalescing waveform study using the simple spark source, as well as the Mach waves simulated by the KZK equation and captured in schlieren images of the jet flow by Willis et al. [12]. The pressure field for a single time step in the LES model at $\phi = 0$ deg is shown in Fig. 12a. Three windows are highlighted, which will be used for subsequent analysis. These windows were generated by interpolating the full LES pressure field onto a grid at a 45 degree angle using bilinear interpolation, so that the near field waveform propagation direction aligns with the axis of the new grid. This process preserved the spatial resolution of $dx = dz = 0.05r_0$ and temporal resolution of $dt = 0.11$ μs. The three windows were then selected to cover different regions where high-amplitude waveforms were visibly overlapping so that a coalescence detection algorithm could be applied. Each window has dimensions of $2.5r_0 \times 12.5r_0$, while pressure data was examined for a dimensionless duration of $\Delta t U_j/D_j = 97.3$ (equivalent to 1000 continuous time steps). For the present study, the boundaries of the window were limited by the bounds of the LES, rather than including data propagated to the far field using other methods described by Pineau and Bogey [5]. Given the proximity of these windows to the jet shear layer (where both evanescent and acoustic waveforms superpose and decay cylindrically), the root-mean-square pressure (σ_p) is calculated along the centerline in each window and compared to cylindrical ($p \propto 1/\sqrt{r}$) and spherical ($p \propto 1/r$) spreading laws in Fig. 12b. For windows 2 and 3, the pressure decay rate is faster than cylindrical decay but slower than spherical decay, while for Window 1, the decay rate is primarily cylindrical.

A. Coalescence Detection Algorithm

Two analysis methods are applied to the data confined by the windows shown in Fig. 12a in order to identify what are believed to be coalescing waveforms. The first is a coalescence detection algorithm, which is similar in principle to the one described by Willis et al. [12]. A second method then employs a new machine learning toolbox that is trained using simulated waveforms.

Starting with the coalescence detection algorithm (CDA), this is based on the one described previously by Willis et al., but with some refinements that align it closer to the shock detection algorithm (SDA) developed by Baars et al. [23]; the algorithm of Baars et al. was developed for microphone measurements, and thus it is better suited for the LES pressure field, as opposed to schlieren intensity. The use of the SDA allows the CDA to identify features that are

propagating and distorting across the selected windows, therefore minimizing the impact of evanescent hydrodynamic features that could be mistakenly identified as coalescing waves. This SDA first identifies features of interest at upstream (z_1) and downstream (z_2) points in a given LES window. Here, z refers to the direction of propagation (at 45 deg) rather than the jet axis, which is denoted as z_j. To simplify the detection, x-averaged pressure values $\bar{p}$ are used to provide a spatially-one-dimensional representation of the field. As developed by Baars et al. [23], the algorithm detects features with the following criteria, based on the pressure standard deviation σ:

$$\frac{\partial \bar{p}(z,t)}{\partial t} \geq \sigma/dt \tag{6}$$

$$\Delta\bar{p}(z,t) \geq 2.7\sigma \tag{7}$$

where dt is the time step for the data and $\bar{p}$ indicates averaging over the x direction. Once potential shock structures have been identified, shock events are related at the upstream and downstream points by the method developed in prior work by Willis et al. [12]. Shocks detected at z_2 and t_2 are related to events dectected by the SDA at z_1 and t_1 through the following simple relationship:

$$t_1 = t_2 - \frac{z_2 - z_1}{c_0} \tag{8}$$

This assumes that the propagation speed c_0 is constant, and that the propagation path is a straight line connecting z_2 to z_1. A steepened waveform resulting from coalescence is expected to have formed from lower amplitude waveforms without shocks at upstream locations. Thus the algorithm outlined by Willis et al. [12] is applied to identify coalescing events rather than propagating shocks as follows:

1) For each shock identified at z_2 and t_2, a time window of $1.95tU_j/D$ centered at t_1 is specified for the time series at z_1.
2) The event is flagged as being a potential contributor to coalescence if no shocks are identified in the window at z_1. This allows the algorithm to distinguish between shocks that propagate between z_1 and z_2 and ones that form due to coalescence between the two points.
3) At time t_1, local maxima with respect to z are identified within a spatial window of $z \times x = 0.25r_0 \times 2.5r_0$ centered at z_1.
4) Events are discarded if they do not satisfy the following criteria, where the indices m and n correspond to any two identified maxima:

$$\sqrt{(z_m - z_n)^2 + (x_m - x_n)^2} > 0.25r_0 \tag{9}$$

$$|z_m - z_n| \leq 0.25r_0 \tag{10}$$

$$p(z_m, x_m, t_1) + p(z_n, x_n, t_1) > \bar{p}(z_2, t_2) \tag{11}$$

Coalescing events that get flagged by the algorithm are then tracked using coordinates that translate at the approximate wave propagation speed. Given the temporal and spatial resolutions of 0.11 μs and $0.05r_0$, respectively, for this LES database an acoustic waveform would be expected to propagate at 343 m/s = 2.2 pixels/frame, which is observed for these detected events. An example of a detected event is presented in Fig. 13, where two waveforms are shown to interact.

From the results of the algorithm, coalescing events were detected in all three windows for the duration of the LES data examined. Specifically, three events were detected in window 1, nine in window 2, and eight in window 3. In order to analyze the low-order makeup of the detected features, a POD analysis using translating coordinates was performed using the tracked waveforms in window 2, where the most potentially coalescing waveforms were detected. The analysis follows the same method outlined in Section II.C, with moving windows encompassing dimensions of $(z' \times x') = (30 \times 50)$ pixels, traversed to $M = 100$ points along the propagation path resulting in 100 partial fields with 1500 spatial points. The first four modes from a POD analysis of the waveforms from Fig. 13 are presented in Fig. 14. In the first mode, a clear structure is observed that corresponds to one of the initial waveforms seen in the first frame of Fig. 13, which also becomes the combined waveform in the last frame of that figure. The second mode appears to correspond to the second waveform that arrives off angle before combining with the first mode. Both the third and fourth modes are less clear, however, the third mode resembles the structure of the second mode. The negative portions of the second and third modes likely contribute to steepening when combined with the first POD mode.

The successful detection of probable coalescence events using the algorithm discussed in this section confirmed that coalescence could be identified in the LES data. To identify additional coalescing events for subsequent analysis, machine learning was applied as a surrogate to the coalescence detection algorithm.

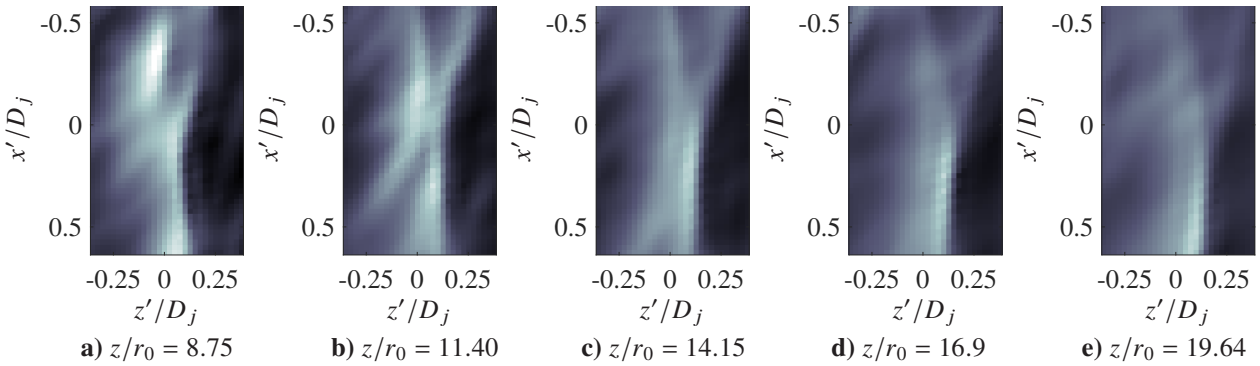

Fig. 13 Spatially resolved windows translating with coalescing waveforms captured in the LES data from window 2.

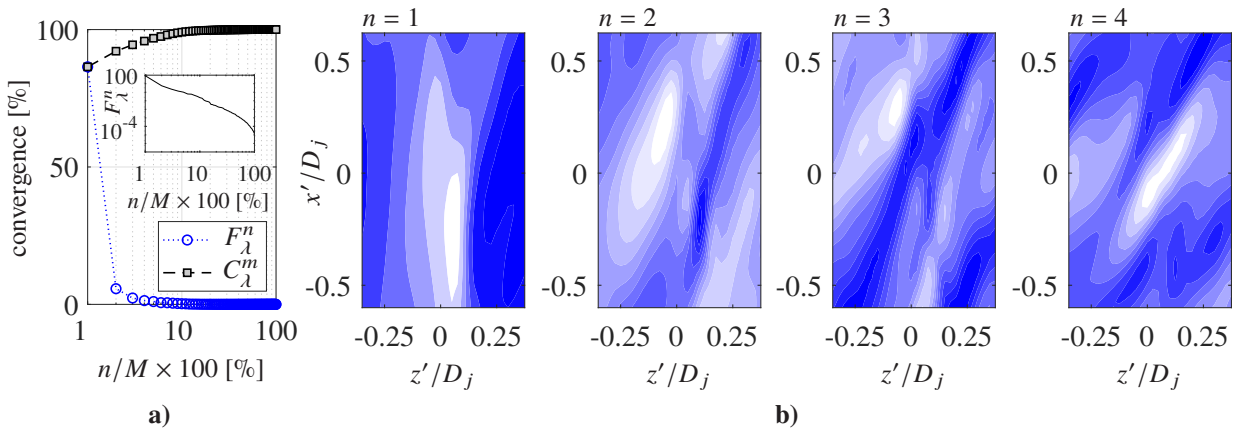

Fig. 14 Translating coordinate POD of detected event shown in Fig. 13. a) Eigenvalue convergence. b) Spatial makeup of the first four POD modes.

B. A Machine Learning Approach for Detecting Coalescence

An alternative approach to detecting shock structures or waveform coalescence in the sound field of these waveform-rich flows is to employ machine learning tools. A flowchart describing the algorithm training and classification process is provided in Fig. 15. Training a network from scratch is a time consuming process that requires a significant amount of data to perform. As such, the algorithm used here applies a transfer learning approach based on the SqueezeNet convolutional neural network [24]. The SqueezeNet network is eighteen layers deep, and was originally trained on the ImageNet database, which provides a rich archive of 3.2 million images for feature identification [25]. The size of ImageNet provides an example of why transfer learning is preferred for this coalescence application; gathering millions of training images of coalescing waveforms would be prohibitory.

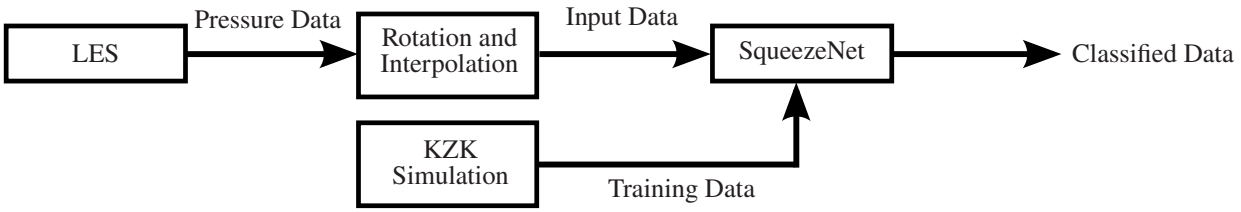

Fig. 15 Flowchart of machine learning process.

The training data used for transfer learning is taken from the KZK simulations of intersecting plane waves, following

the algorithm used in prior work by Willis et al. [12]. The equation solved is given as follows:

$$\frac{\partial p}{\partial z} = \frac{c_0}{2}\int \frac{\partial^2 p}{\partial x^2} d\tau + \frac{\delta}{2c_0^3}\frac{\partial^2 p}{\partial \tau^2} + \frac{\beta}{\rho_0 c_0^3} p \frac{\partial p}{\partial \tau} \tag{12}$$

and is marched forward in the propagation direction z by making use of a dimensionless transformations for all terms [26]. For the source term, two plane waves are steered by angles $\theta_I/2$ and $-\theta_I/2$ with respect to the z axis, thus intersecting initially at angle θ_I in the source plane. These are modeled using the following source condition at $z = 0$:

$$p = p_A \exp\left[-\frac{1}{t_0^2}\left(t - \frac{x}{c_0}\sin\frac{\theta_I}{2}\right)^2 - \left(\frac{x}{a}\right)^{2m}\right] + p_B \exp\left[-\frac{1}{t_0^2}\left(t + \frac{x}{c_0}\sin\frac{\theta_I}{2}\right)^2 - \left(\frac{x}{a}\right)^{2m}\right]. \tag{13}$$

In this source condition, a super-Gaussian spatial distribution $e^{-(x/a)^{2m}}$ is used with $m = 10$ to provide a uniform amplitude in the source plane out to $x \simeq \pm a$ (the characteristic half-width), beyond which the amplitude transitions smoothly to zero. Values for $a = 1$ cm, $p_A = p_B = 500$ Pa and $t_0 = 2$ µs are used in the simulations and were found to produce realistic solutions that compared well to laboratory-scale measurements of Mach waves [12]. A notable difference between the LES model of Pineau and Bogey [5] and the laboratory-scale jet experiments used by Willis et al. [12] is the difference in nozzle exit diameters of $D_j = 0.7$ mm and 2.54 mm, respectively, which changes the jet Reynolds number and acoustic Gol'dberg number. However, the exit velocities of $U_j = 615$ m/s and 624 m/s are quite close. If one assumes that the jet Strouhal number and U_j are approximately the same, then the ratio of characteristic frequencies is inversely proportional to the ratio of nozzle diameters. This is used to adjust the scale of the KZK training data to approximate the LES database through scaling based on D_j.

The training data set mainly consisted of intersecting waveforms simulated with θ_I ranging from 1 to 40 degrees. Based on prior results of Willis et al. [12], it was determined that, for the parameters listed above, steepening was significant when compared to a single waveform for intersection angles up to 20 degrees. Thus, training data was split into three categories. The first comprised waveforms intersecting at $\theta_I \leq 20$ deg, labeled "coalescing," while the second was for intersecting waveforms with $20 < \theta_I \leq 40$ deg labeled "intersecting." Examples of waveforms from these first two categories are shown in Fig. 16. As for the third and final category, early trials demonstrated difficulties

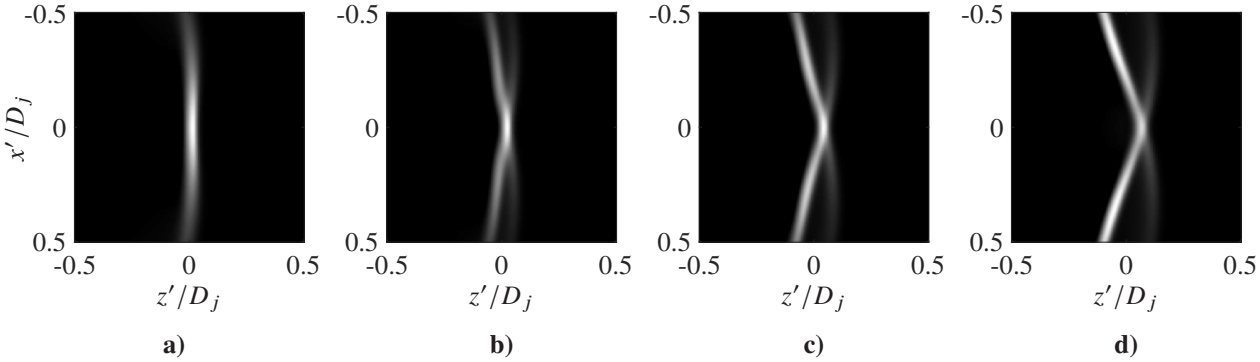

Fig. 16 KZK algorithm images used for network training. a,b) Waveforms in the "coalescing" category for a) $\theta_I = 5$ **deg and b)** $\theta_I = 15$ **deg. c,d) Waveforms in the "intersecting" category for c)** $\theta_I = 25$ **deg and d)** $\theta_I = 35$ **deg.**

in distinguishing intersecting waveforms from non-intersecting waveforms. Therefore, simulations were carried out with the following new source term for non-intersecting, identical plane waves of amplitude $p_A = p_B = 500$ Pa, and separated by a time delay of t_D:

$$p = p_A \exp\left[-\frac{(t + t_D/2)^2}{t_0^2} - \left(\frac{x}{a}\right)^{2m}\right] + p_B \exp\left[-\frac{(t - t_D/2)^2}{t_0^2} - \left(\frac{x}{a}\right)^{2m}\right] \tag{14}$$

This provided the basis for the third category comprising "non-intersecting" waveforms, which were simulated in the same manner as the intersecting categories. In Eq. (14), values for t_D/t_0 between 2 and 20 were used, along with a case

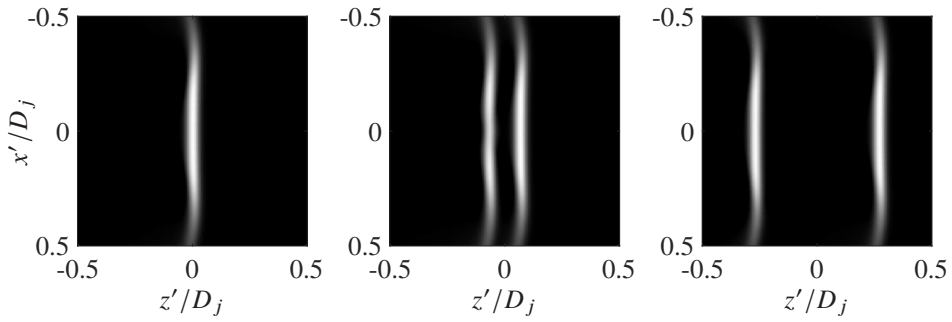

Fig. 17 Example images used as training data for a) a single waveform, b) non-intersecting waves with a time delay of $5t_0$, and c) non-intersecting waves with $20t_0$ time delay.

Network	Training Image Size	Training $z_{\max}$	Final Validation Accuracy	Final Validation Loss
1	$1D_j$	$10D_j$	91.1%	0.19
2	$2D_j$	$10D_j$	90.3%	0.25
3	$1D_j$	$5D_j$	90.6%	0.23

Table 2 Parameters for training data sets used for preparation of the convolutional neural network.

with $p_B = 0$ to account for propagation of a single waveform. Images from the "non-intersecting" noise category are shown in Fig. 17. The waveforms collected for all three categories were then normalized by the maximum pressures of their respective windows, while only positive pressure values were retained in the training images in order to simplify features for the machine learning algorithm. This normalization was applied to the LES data as well, in order to match training data with test data.

Using the images obtained from simulated KZK waveforms, and separated into their respective categories, multiple sets of training data were assembled with different properties, as outlined in Table 2 and described below. These training sets were used to train three distinct networks, with the goal of determining how to best format the training data to improve network performance.

1) Network 1 was trained on images of size $(z, x) = (1D_j, 1D_j)$ captured at incremental distances of $0.5D_j$ out to a distance of $z_{\max} = 10D_j$, resulting in 400 images per category.
2) Network 2 was trained on images of size $(z, x) = (2D_j, 2D_j)$ captured at incremental distances of $0.5D_j$ out to a distance of $z_{\max} = 10D_j$, resulting in 400 images per category.
3) Network 3 was trained on images of size $(z, x) = (1D_j, 1D_j)$ captured at incremental distances of $0.5D_j$ out to a distance of $z_{\max} = 5D_j$, resulting in 200 images per category.

For all three networks, images were scaled to a window size with 227×227 pixel resolution in order to match the input requirements for SqueezeNet. Training images were then augmented by randomly shifting their location along the direction of propagation by up to ±50 pixels (equivalent to $0.22D_j$ for an image size of $1D_j$), rotating them ±20 degrees, and rescaling them up to a factor of two in order to improve performance. Thirty percent of each set was reserved for validation. With these parameters, the SqueezeNet network was then re-trained over 20 epochs, and the iteration with lowest validation loss was taken as the output network.

The retrained networks were then applied to the LES windows, with frames selected for classification over the span of the window and 1000 time steps. The classified LES images had dimensions of $(x, z') = (2.5r_0, 2.5r_0)$, where z is the direction of wave propagation following Fig. 1. Images were obtained at incremental distances of $1.25r_0$ in the z direction, resulting in nine images per time step per window. Examples of classified images are shown in Figure 18, along with its most likely classification and probability. It is worth noting that the frame in Figure 18b corresponds to the event detected by the coalescence detection algorithm in Figure 13.

For all three networks, the vast majority of frames were classified as intersecting, which is expected due to the waveform-rich region of the flow. The structures classified as"coalescing" typically exhibited interaction between multiple waveforms, or the presence of a single waveform with significantly higher amplitude than other structures in

the same frame. The number of images classified as "coalescing" with a probability above 70% were counted in each window and network, and the results are presented in Fig. 19 (the results for the "intersecting" and "non-intersecting" categories are neglected here for brevity). The highest number of images were classified as "coalescing" for Network 1, which was concluded to have the best performance. The stark differences in classification numbers demonstrate how minor differences in the training data can significantly impact the resulting algorithm, with the algorithm being more sensitive to the mismatch between frame sizes exhibited by Network 2 compared to variation in the propagation distance as exhibited by Network 3.

All three algorithms share a common trend across the three windows in that more frames were classified as "coalescing" for the windows located farther downstream. This complements the findings using the coalescence detection algorithm discussed in section III.A, which detected the fewest coalescing events in Window 1. Conversely, Window 1 had the highest number of frames classified as"non-intersecting" compared to Windows 2 and 3. No clear trend is observed in how many frames were classified for each distance from the jet, but the results for Network 1 display a shared increase in the number of detected coalescing events at $z/r_0 = 3.75$ and 8.75 as seen in Fig. 19. It is also unclear if our machine learning algorithm can distinguish between propagating waveforms and evanescent structures, especially close to the jet where a greater number of hydrodynamic fluctuations would be expected. A retraining of the neural network using additional influences from the shock detection algorithm or waveform tracking methods might alleviate this discrepancy and will be considered in future work.

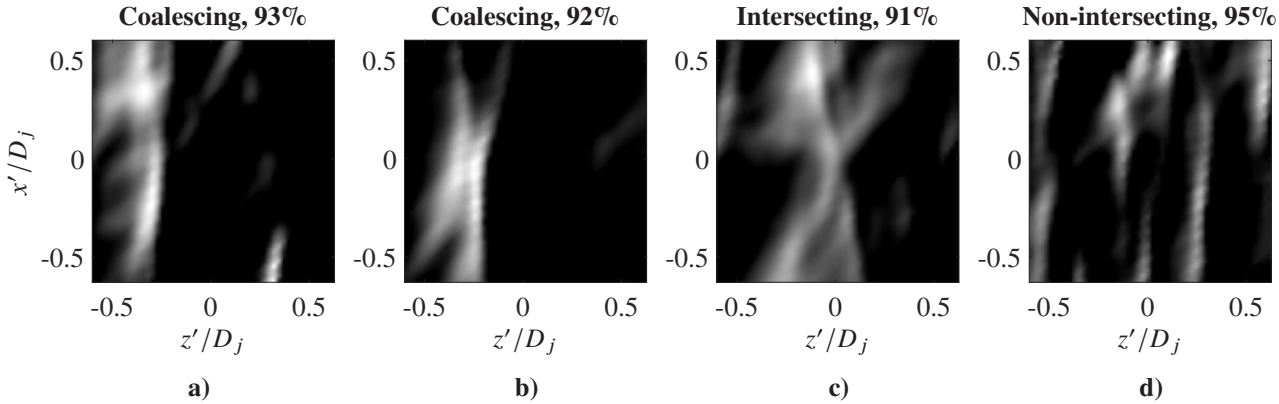

Fig. 18 Example LES frames that have been classified by Network 1, along with the assigned probability for that classification.

IV. Conclusions

Following the determination, based on numerical simulations in the prior work, that the coalescence process could significantly impact waveform steepening [12], the present study has developed both experimental and computational methods for examining coalescence between waves in air. These methods are designed to overcome shortcomings of working with a lab-scale jet by generating coalescing waveforms in a repeatable manner using a spark source, and by analyzing pressure data directly in a simulated jet flow.

This study presents two simplified experiments that were designed and conducted to allow for the analysis of coalescence-induced steepening effects on spark-generated waveforms in air. The first, based on the shared boundary condition between a rigid surface and symmetric intersection, captured coalescing waveforms using flush-mounted microphones along the surface, which were compared to waveforms measured in the free field. These measurements demonstrated that the waveforms incident on the surface were steeper, as characterized by skewness of the pressure time derivative. The second experiment placed the spark source in an enclosure designed to split the resulting waveform into two separate waveforms that intersected as they propagated. Schlieren intensity was used to characterize the waveform steepening to avoid microphone limitations. The coalescing waveforms exhibited sharper, higher-amplitude peaks along with a higher ratio of peak positive to peak negative intensity close to the source, all indicators of greater steepness compared to a single waveform emanated from just one of the enclosure's vents.

To provide an additional method for analysis of coalescing waveforms, an LES database described by Pineau and Bogey [5] was examined to identify examples of coalescing waves. A coalescence algorithm similar to that outlined

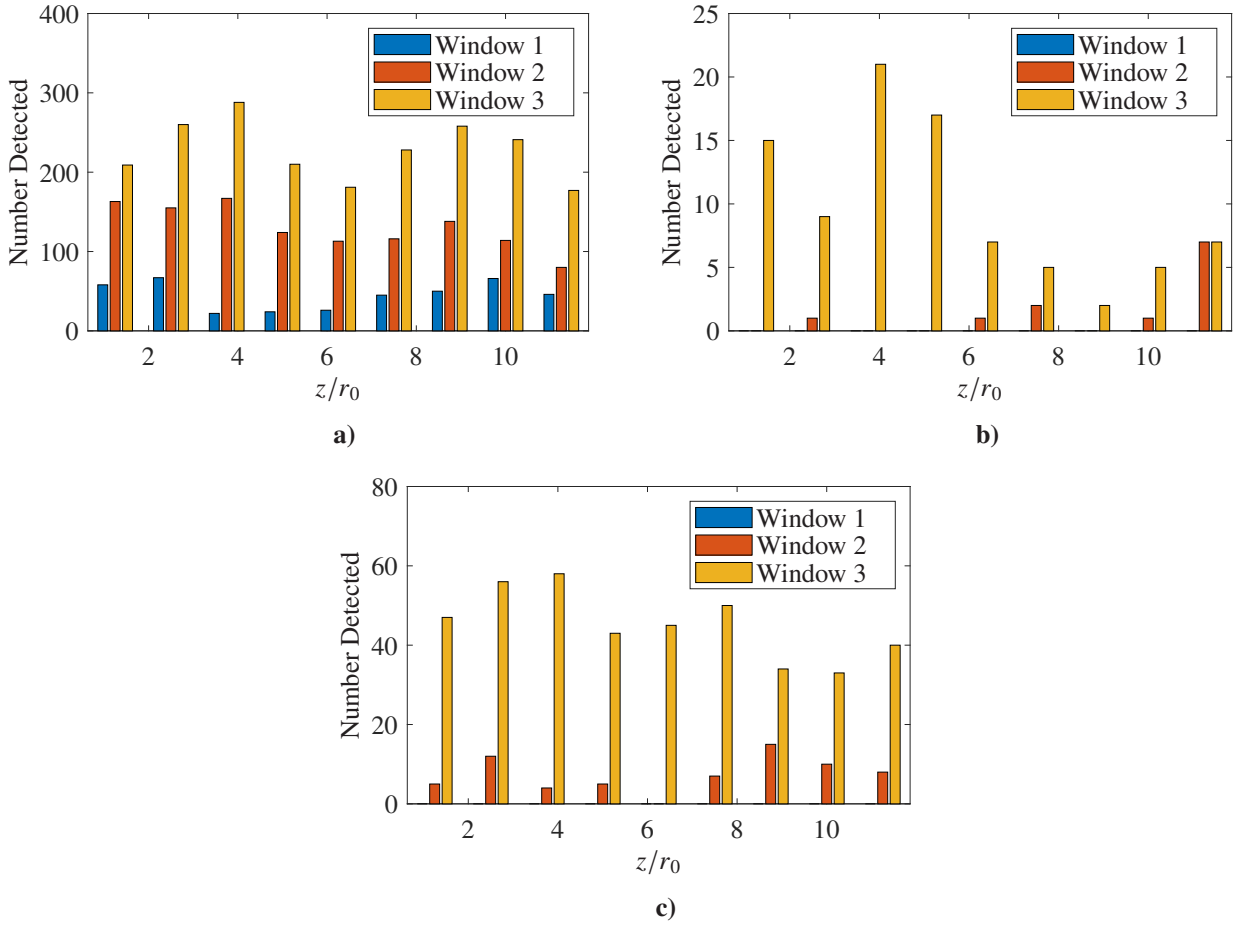

Fig. 19 Count of images classified as "coalescing" for LES windows as determined by a) Network 1, b) Network 2, and c) Network 3, with training parameters described in Table 2.

in the prior work [12] was applied to three windows of the LES pressure data close to the jet, each aligned at 45 deg to match the expected propagation direction for Mach waves. The algorithm detected potential coalescing events for all three windows, with a higher number detected in the windows located farther downstream. The algorithm isolated some clear examples of potential coalescence events, such as in Fig. 13. However, additional methods were found necessary for isolating coalescence events in the waveform-rich LES data set.

A machine learning algorithm was developed using transfer learning along with the SqueezeNet convolutional neural network [24]. Multiple training data sets were constructed using waveform simulations carried out by a numerical model of the KZK equation, with waveforms separated into categories of "coalescing," "intersecting," and "non-intersecting" for machine learning classification. The machine learning algorithm was then applied to the 45 deg windows from the LES pressure data. Network 1, which was trained on images with a size of $(z, x) = (1D_j, 1D_j)$ and captured at distances out to $10D_j$, detected the highest number of coalescence events. All three networks classified more frames as "coalescing" for the windows farther downstream from the jet nozzle, while more frames were classified as "non-intersecting" for the window furthest upstream. This trend was shared with the algorithm discussed in Section III.A. Overall, the success of Network 1 in detecting potential events with these trends, including some overlap with the non-machine-learning approach as demonstrated by Figs. 13 and 18, provide confidence that the approach does have merit. However, the strong sensitivity to training parameters, as indicated by the large differences in behavior between the three networks, makes the application of machine learning toward this problem difficult.

Acknowledgements

The first author would like to acknowledge support from the Chester M. McKinney Graduate Fellowship in Acoustics at the Applied Research Laboratories of the University of Texas at Austin. The numerical data analyzed in this work were obtained using the HPC resources of PMCS2I (Pôle de Modélisation et de Calcul en Sciences de l'Ingénieur et de l'Information) of École Centrale de Lyon.

References

[1] Baars, W. J., Murray, N. E., and Tinney, C. E., "A proper framework for studying noise from jets with non-compact sources," *Journal of Fluid Mechanics*, Vol. 929, No. A23, 2021, pp. 1–32. https://doi.org/10.1017/jfm.2021.837.

[2] Nichols, J. W., Lele, S. K., Ham, F. E., Martens, S., and Spyropoulos, J., "Crackle noise in heated supersonic jets," *Journal of Engineering for Gas Turbines and Power*, Vol. 135, No. 5, 2013, p. 051202. https://doi.org/10.1115/1.4007867.

[3] Buchta, D. A., and Freund, J., "The near-field pressure radiated by planar high-speed free-shear-flow turbulence," *Journal of Fluid Mechanics*, Vol. 832, 2017, pp. 383–408.

[4] Pineau, P., and Bogey, C., "Temperature effects on convection speed and steepened waves of temporally developing supersonic jets," *AIAA Journal*, Vol. 58, No. 3, 2020, pp. 1227–1239.

[5] Pineau, P., and Bogey, C., "Numerical investigation of wave steepening and shock coalescence near a cold Mach 3 jet," *Journal of the Acoustical Society of America*, Vol. 149, No. 1, 2021, pp. 357–370.

[6] Ffowcs Williams, J., Simson, J., and Virchis, V., "'Crackle': an annoying component of jet noise," *Journal of Fluid Mechanics*, Vol. 71, 1975, pp. 251–271.

[7] Baars, W. J., Tinney, C. E., Wochner, M. S., and Hamilton, M. F., "On cumulative nonlinear acoustic waveform distortions from high-speed jets," *Journal of Fluid Mechanics*, Vol. 749, No. 12, 2014, pp. 331–366. https://doi.org/10.1017/jfm.2014.228.

[8] Baars, W. J., Tinney, C. E., and Hamilton, M. F., "Piecewise-spreading regime model for calculating effective Gol'dberg numbers for supersonic jet noise," *AIAA Journal*, Vol. 54, No. 9, 2016, pp. 2833–2842. https://doi.org/10.2514/1.j054790.

[9] Gee, K. L., Sparrow, V. W., Atchley, A., and Gabrielson, T. B., "On the perception of crackle in high-amplitude jet noise," *AIAA Journal*, Vol. 45, No. 3, 2007, pp. 593–598.

[10] Fiévet, R., Tinney, C. E., Baars, W. J., and Hamilton, M. F., "Coalescence in the sound field of a laboratory-scale supersonic jet," *AIAA Journal*, Vol. 54, No. 1, 2016, pp. 254–265. https://doi.org/10.2514/1.j054252.

[11] Hamilton, M. F., "Effective Gol'dberg number for diverging waves," *The Journal of the Acoustical Society of America*, Vol. 140, No. 6, 2016, pp. 4419–4427. https://doi.org/10.1121/1.4968787.

[12] Willis, W. A., Cormack, J. M., Tinney, C. E., and Hamilton, M. F., "Reduced-order models of coalescing Mach waves," *AIAA SCITECH 2022 Forum*, 2022. https://doi.org/10.2514/6.2022-1792.

[13] Lipkens, B., and Blackstock, D. T., "Model experiment to study sonic boom propagation through turbulence. Part I: General results," *The Journal of the Acoustical Society of America*, Vol. 103, No. 1, 1998, pp. 148–158. https://doi.org/10.1121/1.421114.

[14] Hay, T. A., Valdez, J. A., Tinney, C. E., Hamilton, M. F., and Schram, C., "Sampling artifacts in quantitative schlieren," *25th AIAA/CEAS Aeroacoustics Conference*, Vol. 2019-2635, 2019, pp. 1–13. https://doi.org/10.2514/6.2019-2635.

[15] Tinney, C. E., Valdez, J. A., Meier, H., and Ruf, J. H., "Laboratory scale testing of ignition overpressure for space launch pad environments," *25th AIAA/CEAS Aeroacoustics Conference*, Vol. 2019-2635, 2019, pp. 1–15. https://doi.org/10.2514/6.2019-2413.

[16] Karzova, M. M., Khokhlova, V. A., Salze, E., Ollivier, S., and Blanc-Benon, P., "Mach stem formation in reflection and focusing of weak shock acoustic pulses," *The Journal of the Acoustical Society of America*, Vol. 137, No. 6, 2015. https://doi.org/10.1121/1.4921681.

[17] Pestorius, F. M., and Blackstock, D. T., "Propagation of finite-amplitude noise," *Proc. of the 1973 International Symposium on Nonlinear Acoustics*, edited by L. Bjørnø, IPC Science and Technology Press Ltd., Guildford, Surrey, England, 1974, pp. 24–29. Since the proceedings paper is hard to access, see a reproduction of Fig. 5 in Pestorius and Blackstock as Fig. 2 of K. L. Gee, "On the contributions of David T. Blackstock to understanding nonlinear propagation of jet noise," Proc. Meet. Acoust. Vol. 45, 045001 (2022).

[18] Yuldashev, P., Ollivier, S., Averiyanov, M., Sapozhnikov, O., Khokhlova, V., and Blanc-Benon, P., "Nonlinear propagation of spark-generated N-waves in air: Modeling and measurements using acoustical and optical methods," *The Journal of the Acoustical Society of America*, Vol. 128, No. 6, 2010, pp. 3321–3333. https://doi.org/10.1121/1.3505106.

[19] Lumley, J., "The structure of inhomogenous turbulent flows," *Proceedings of the International Colloquium on the Fine Scale Structure of the Atmosphere and its Influence on Radio Wave Propagation, ed. Yaglom A. M., and Tatarski V. I. Doklady Akademii Nauk SSSR, Moscow*, Vol. 45, 1967, pp. 166–178.

[20] Berkooz, G., Holmes, P., and Lumley, J. L., "The proper orthogonal decomposition in the analysis of turbulent flows," *Annual Review of Fluid Mechanics*, Vol. 25, 1993, pp. 539–575.

[21] Tinney, C. E., Glauser, M. N., and Ukeiley, L. S., "Low-dimensional characteristics of a transonic jet. Part 1. Proper orthogonal decomposition," *Journal of Fluid Mechanics*, Vol. 612, 2008, pp. 107–141. https://doi.org/10.1017/S0022112008002978.

[22] Tinney, C. E., "Sparse Biorthogonal Decomposition," *AIAA SciTech 2021 Forum*, Vol. 2021-1851, 2021, pp. 1–18.

[23] Baars, W. J., and Tinney, C. E., "Shock-structures in the acoustic field of a Mach 3 jet with crackle," *Journal of Sound and Vibration*, Vol. 333, No. 12, 2014, pp. 2539–2553. https://doi.org/10.1016/j.jsv.2014.01.008.

[24] Iandola, F. N., Han, S., Moskewicz, M. W., Ashraf, K., Dally, W. J., and Keutzer, K., "SqueezeNet: AlexNet-level accuracy with 50x fewer parameters and <0.5MB model size," 2016. https://doi.org/10.48550/ARXIV.1602.07360, URL https://arxiv.org/abs/1602.07360.

[25] Deng, J., Dong, W., Socher, R., Li, L.-J., Li, K., and Fei-Fei, L., "ImageNet: A large-scale hierarchical image database," *2009 IEEE Conference on Computer Vision and Pattern Recognition*, 2009, pp. 248–255. https://doi.org/10.1109/CVPR.2009.5206848.

[26] Shull, D. J., Kim, E. E., Hamilton, M. F., and Zabolotskaya, E. A., "Diffraction effects in nonlinear Rayleigh wave beams," *The Journal of the Acoustical Society of America*, Vol. 97, No. 4, 1995, pp. 2126–2137. https://doi.org/10.1121/1.412005.